

# Bifurcation and metastability in a new one-dimensional model for martensitic phase transitions

Anna Vainchtein\*, Timothy J. Healey, Phoebus Rosakis

*Department of Theoretical and Applied Mechanics, Cornell University, Ithaca, NY 14853, USA*

## Abstract

Materials undergoing stress-induced martensitic phase transitions often form complex twinned microstructures with multiple phase boundaries. They also exhibit hysteretic mechanical behavior. We propose and analyze a one-dimensional model for twinning. We consider two elastic bars coupled by a system of continuously distributed linear springs. One of the bars has a two-well nonconvex elastic energy density that models a two-variant martensitic phase. The other bar is linearly elastic and is meant to model the parent austenite phase. Interfacial energy is modeled by a strain-gradient term. Various types of boundary conditions model parameter-dependent loading. A local bifurcation analysis shows that local energy minima (metastable states) often involve a large number of phase boundaries. This is confirmed by the global-bifurcation diagrams obtained numerically. We observe that this microstructure emerges via both sudden (finite) and gradual (infinitesimal) phase nucleation. We propose an energetic argument that predicts hysteresis in overall load-deformation behavior due to metastability of multiple equilibria. A limiting case with zero interfacial energy is treated analytically, yielding global solution diagrams. © 1999 Elsevier Science S.A. All rights reserved.

## 1. Introduction

Stress-induced martensitic phase transitions in crystalline solids involve a transformation from a high-symmetry *austenite* phase to a lower-symmetry *martensitic* phase. The martensite can exist in multiple forms related to each other by symmetry. These are called *twin variants*. For example, the copper–aluminum–nickel alloy transforms from cubic austenite to orthorhombic martensite that has six variants. The coexistence of two variants involves an interface separating them, known as a *twin boundary*. Under applied stress, materials undergoing martensitic transformation form complex twin microstructures consisting of many alternating layers of two or more variants [4,13,15]. They also exhibit a markedly hysteretic behavior under cyclic loading [1,4,12–15].

By now it is common to employ models of martensitic phase transitions that involve a nonconvex elastic energy density (see e.g. [2,8,10,19]). The relevance of this approach in statics was initially demonstrated by Ericksen [6]. He considered a one-dimensional equilibrium problem for a nonlinearly elastic bar with a nonconvex energy density. His approach was to study minimization of the energy functional

$$E = \int_0^1 f(u') dx, \quad (1)$$

where  $f(u')$  is a two-well elastic energy density,  $u(x)$  is the axial displacement of the point with reference position  $x \in [0,1]$  (the undeformed configuration of the bar), and  $u'(x)$  is the strain. For example, we may choose

\* Corresponding author. e-mail: vainchte@tam.cornell.edu

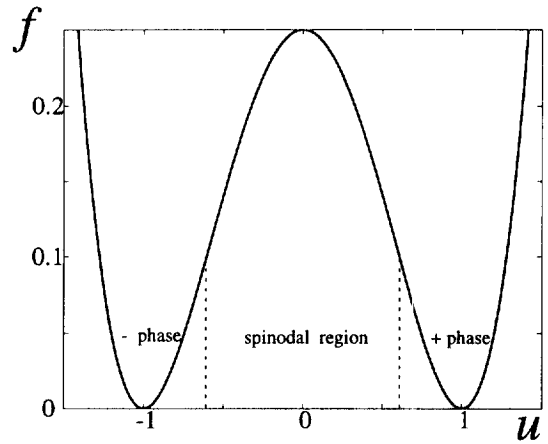


Fig. 1. The energy density function  $f(u')$ .

$$f(u') = \frac{1}{4} [(u')^2 - 1]^2, \tag{2}$$

the graph of which is depicted in Fig. 1. The two wells correspond to different material phases. Throughout this paper, we refer to the interval of strains  $\{u': u' > 1/\sqrt{3}\}$  as the + or *high-strain phase* and the interval  $\{u': u' < -1/\sqrt{3}\}$  as the - or *low-strain phase*. Note that  $f(u')$  given by (2) is convex for strains  $u'$  in the  $\pm$  phase intervals. The interval of strains  $\{u': f''(u') \leq 0\} = [-1/\sqrt{3}, 1/\sqrt{3}]$ , where  $f$  is locally concave, is called the *spinodal region*. By minimizing the functional (1) subject to the boundary conditions

$$u(0) = -d/2, \quad u(1) = d/2, \tag{3}$$

Ericksen shows that for each  $d$  in  $[-1, 1]$ , apart from the homogeneous solution  $u(x) = dx - d/2$ , which is unstable for  $d \in [-1/\sqrt{3}, 1/\sqrt{3}]$ , there is an uncountable infinity of inhomogeneous, energy-minimizing solutions. Each of the latter involves a phase mixture;  $u$  is continuous but piecewise linear, with  $u' = +1$  or  $-1$  almost everywhere. Only the measures of the two subsets of the bar where  $u' = 1$  or  $u' = -1$  are determined by  $d$ . The distribution and number of interfaces (discontinuities of  $u'$ ) are arbitrary. Accordingly, the global energy minimizer may have an arbitrarily high number of phase boundaries, which is not physically realistic.

One way to overcome this shortcoming is to introduce a strain-gradient term penalizing the formation of sharp interfaces:

$$E = \int_0^1 [f(u') + \alpha u'^2] dx, \tag{4}$$

where  $\alpha > 0$  is a constant nonlocality coefficient. For studies of this problem see [3,9,17]. Solutions to the corresponding Euler–Lagrange equations are now smooth; all discontinuities in  $u'$  are replaced by transition layers of thickness proportional to  $\sqrt{\alpha}$ . One may view the strain-gradient term as modeling the effect of interfacial energy. It was shown in [3] that the minimizer of (4) can have at most one phase boundary. However, experimental observations such as [4] often show states with multiple interfaces.

This led some researchers [10,11,18–20] to introduce an interaction of the bar with an elastic foundation (a continuous distribution of linear noninteracting springs), and thus to minimize the functional

$$E = \int_0^1 [f(u') + \alpha u'^2 + \beta u^2] dx, \tag{5}$$

where  $\beta > 0$  is the elastic foundation stiffness. Physically, the effect of the elastic foundation attempts to mimic the interaction of different phases in higher dimensions. There, the low energy states at the bottoms of energy wells of different phases are often incompatible with each other or with the boundary conditions.

While the interfacial energy term tends to suppress rapid strain variations, the elastic foundation enhances

them, since oscillations in strain allow the average displacement to remain small. The competition of these two terms results in minimizers of the energy with a finite number of interfaces.

In this paper we propose and analyze a new one-dimensional model for twinning in an austenite–martensite mixture. We consider two coupled bars acting in parallel; one nonlinearly elastic bar is meant to model two possible variants of martensite (twins), while the other linearly elastic bar corresponds to the austenite phase. Displacement or traction boundary conditions are prescribed at the ends of each bar. Let  $x \in [0, 1]$  be a reference coordinate of a point in either of the bars (see Fig. 2). The bars interact via a continuous distribution of linear springs. Let  $u$  and  $v$  denote the displacements in the upper and lower bars, respectively. The upper bar has the two-well elastic energy density (2). The lower bar is linearly elastic, with energy density  $\mu v'^2$ ; here  $\mu > 0$  is a constant elastic modulus. The preferred zero-energy states  $u' = \pm 1$  of the upper bar (martensite) are thus different from the preferred state  $v' = 0$  for the lower, austenitic bar. This models the kinematic incompatibility of these two phases in most crystalline alloys, which is responsible for microstructure formation in martensite. We also include the usual interfacial energy (strain-gradient) term  $\int_0^1 \alpha u''^2 dx$ . The energy stored in the springs coupling the bars is  $\int_0^1 \beta (u - v)^2 dx$ , where  $\beta > 0$  is a constant spring stiffness. The total potential energy of the system is then

$$E = \int_0^1 [f(u') + \alpha u''^2 + \mu v'^2 + \beta (u - v)^2] dx. \tag{6}$$

We consider three types of boundary conditions.

*Coupled-Bar Model I.* Displacement boundary conditions are prescribed for both bars:

$$u(0) = -d/2, \quad u(1) = d/2, \quad v(0) = -d/2, \quad v(1) = d/2. \tag{7}$$

*Coupled-Bar Model II.* We prescribe displacement boundary conditions for the upper, and traction-free boundary conditions for the lower bar:

$$u(0) = -d/2, \quad u(1) = d/2, \quad v'(0) = 0, \quad v'(1) = 0. \tag{8}$$

*Coupled-Bar Model III.* Displacement boundary conditions are prescribed for the lower bar and traction-free boundary conditions for the upper one:

$$f'(u'(0)) - 2\alpha u'''(0) = 0, \quad f'(u'(1)) - 2\alpha u'''(1) = 0, \quad v(0) = -d/2, \quad v(1) = d/2. \tag{9}$$

Here  $d$  is the applied end displacement. Observe in (9) that the stress in the upper bar takes the form  $f'(u') - 2\alpha u''$ . We seek local minimizers of (6) subject to boundary conditions (7), (8) or (9) in the corresponding models.

In each model, the equilibria  $(u, v)$  must belong to  $(C^4(0, 1), C^2(0, 1))$  and satisfy the system of Euler–Lagrange equations

$$\begin{cases} f''(u')u'' - 2\alpha u''' - 2\beta(u - v) = 0, \\ \mu v'' + \beta(u - v) = 0, \end{cases} \tag{10}$$

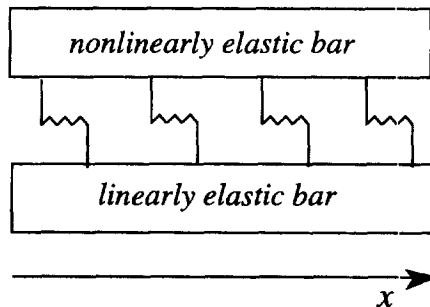


Fig. 2. Schematic of coupled bars.

the natural boundary conditions

$$u''(0) = u''(1) = 0, \quad (11)$$

and the corresponding boundary conditions (7), (8) or (9). Here,  $f(u')$  is given by (2). The natural boundary conditions (11) arise from the strain-gradient term and require that the couple stresses vanish at the ends of the upper bar.

We remark that system (10) is equivalent to a single integro-differential equation obtained by finding a Green's function for  $(10)_2$  and expressing  $v$  in terms of  $u$ . For model I, the integral equation is given by

$$f''(u')u'' - 2\alpha u'''' - 2\beta u + 2\beta \left[ \frac{d(\sinh(sx) + \sinh(s(x-1)))}{2\sinh(s)} - \frac{\beta}{\mu} \int_0^1 u(\xi)G(\xi, x) d\xi \right], \quad (12)$$

where  $s = \sqrt{\beta/\mu}$  and

$$G(\xi, x) = \begin{cases} (\sinh(s(x-1))\sinh(s\xi))/(s\sinh(s)) & \text{for } 0 \leq \xi < x, \\ (\sinh(sx)\sinh(s(\xi-1)))/(s\sinh(s)) & \text{for } x < \xi \leq 1, \end{cases} \quad (13)$$

is the Green's function. The integral term in (12) reflects the nonlocal interaction in this model.

In addition to models I, II, III, we also consider an interesting asymptotic version of model I, viz., we let  $\beta/\mu \rightarrow 0$  in  $(10)_2$ . Then,  $(7)_3$  and  $(7)_4$  dictate that the lower bar have displacement  $v(x) = d(x - 1/2)$ , with constant strain  $v'(x) = d$ . This model will be called the *pseudorigid foundation model*. The total potential energy reduces to

$$E = \int_0^1 [f(u') + \alpha u''^2 + \beta (u - d(x - 1/2))^2] dx + g(d), \quad (14)$$

where  $g(d)$ , the elastic energy of the lower bar, can be any convex function of  $d$ . The equation governing the deformation in the upper bar will then be

$$f''(u')u'' - 2\alpha u'''' - 2\beta (u - d(x - 1/2)) = 0. \quad (15)$$

In addition, the natural boundary conditions (11) and boundary conditions  $(7)_{1,2}$  must be satisfied.

It is also worth noting that if  $\beta = 0$  in (10), model II reduces to the no-foundation model associated with (4), (cf. [3,9,17]). Moreover, if we again let  $\beta/\mu \rightarrow 0$  in  $(10)_2$  in model II, we then obtain the model associated with (3), (5) (cf. [10,11,18–20]).

Our goals here are the same as those of [19] and [20], in which the elastic-foundation problem associated with (5) was studied. We are interested in obtaining branches of local energy minima (metastable equilibria) as the end displacement  $d$  varies. Our tools are those of bifurcation theory and numerical branch tracing, accompanied by the determination of stability via the second variation. In this way we capture basic mechanisms of hysteresis associated with cyclic variations in  $d$ , which are typically missed by the usual approach of direct global energy minimization [8].

In addition to our belief that (6) and (14) provide better one-dimensional models for twinning than (5), both model I and the pseudorigid foundation model have the virtue of admitting a trivial homogeneous solution for all values of  $d \in [-1, \infty)$ . This fact allows a detailed local bifurcation analysis, which we present in Section 2. For both models we find physically reasonable regimes of the material parameters for which stable higher-mode solution branches bifurcate earlier than lower modes. Similar phenomena are observed in the buckling of plates and bars on elastic foundations [16]. In the context of our models, we obtain stable solutions possessing a large number of phase boundaries, which represents a substantial improvement on the single-phase-boundary results of [3,9,17] associated with (4).

In Section 4 we present global-numerical results for models I–III and the pseudorigid-foundation model. As in [19,20], we find that the energy at the *global* minimum is not a smooth function of the prescribed end displacement  $d$ , but exhibits corners. This function is called the *lowest energy envelope*. Each corner corresponds to a *finite nucleation event*. By that we mean the following: suppose that the bar is initially in the low-strain phase. At a critical value of end displacement corresponding to a corner in the lowest energy envelope, an interval of *finite* length with strains in the high-strain phase suddenly appears in the interior or at the end of the bar. As in [20], we observe a different, *infinitesimal nucleation* pattern: as the prescribed end

displacement is increased, an initially infinitesimal interval with strain in the spinodal region appears in the bar interior and grows *gradually*. This *pretransitional* nucleus is stable (i.e. the corresponding solution is a local minimizer of the energy functional), although it involves strain in the spinodal region. Infinitesimal nucleation events correspond to smooth transitions on the lowest energy envelope

Further, we introduce an energetically motivated strategy for switching between branches of local minima. As a result we obtain hysteresis loops in the overall end-load *versus* end-displacement diagrams resulting from the coupled-bar models.

In Section 5, we consider the case without interfacial energy, viz.  $\alpha = 0$ . Note that in this case (10) has singularities, since  $f''(\pm 1/\sqrt{3}) = 0$ , (cf. [2]). In particular, the standard path-following approach employed in Section 4 may fail. Instead, we approximate the energy density  $f$  by piecewise-smooth quadratic polynomials, and (10) becomes piecewise-linear. We then obtain solutions analytically by enforcing appropriate jump conditions. In this way, we construct global solution diagrams comparable to those of Section 4 for the important limiting case  $\alpha = 0$ . We summarize our conclusions in Section 6.

## 2. Results of local bifurcation analysis

Both the pseudorigid foundation model and model I admit trivial homogeneous solutions not possible in the other models. This allows a local bifurcation analysis, which we now present.

Consider first the pseudorigid foundation model, in which equilibria are governed by (15), (7)<sub>1,2</sub> and (11). The problem has the trivial solution  $u = d(x - 1/2)$ . Linearizing (15) about this solution, we obtain

$$\begin{cases} f''(d)\eta'' - 2\alpha\eta'''' - 2\beta\eta = 0, \\ \eta(0) = \eta(1) = \eta'(0) = \eta'(1) = 0. \end{cases} \tag{16}$$

The eigenvalues  $d_n$  of the problem (16) are roots of

$$f''(d_n)(n\pi)^2 + 2\alpha(n\pi)^4 + 2\beta = 0 \tag{17}$$

with corresponding eigenfunctions  $\eta_n = \sin(n\pi x)$ . One can show that  $d_n$  satisfying (17) correspond to bifurcation points, with local nontrivial solution

$$u_n(x) = dx - \frac{d}{2} + \varepsilon \sin(n\pi x) + o(\varepsilon) \tag{18}$$

and

$$d = d_n + O(\varepsilon^2) \tag{19}$$

in a small  $\varepsilon$ -neighborhood of the bifurcation point  $(u, d) = (d_n(x - 1/2), d_n)$ . Here

$$\varepsilon = \int_0^1 \sqrt{2} \sin(n\pi x) \left( u - dx + \frac{d}{2} \right) dx \tag{20}$$

and  $n$  is a mode number.

Assume that in the spinodal region  $f''(d)$  monotonically decreases, reaches a negative minimum at some  $d_*$  ( $d_* = 0$  when  $f(u')$  is given by (2)) and then monotonically increases. Then, for each  $n$ , the bifurcation points come in pairs,  $d_n^1 < d_*$  and  $d_n^2 > d_*$  satisfying (17). From (17) it follows that  $d_n$  satisfy

$$f''(d_n) = -[2\beta(1/n\pi)^2 + 2\alpha(n\pi)^2] < 0. \tag{21}$$

Fix a value of  $n$  and assume that

$$f''(d_*) \leq -2\alpha(\pi n)^2 \tag{22}$$

to ensure the existence of solutions to (21) for  $\beta = 0$ . As we increase  $\beta$ ,  $f''(d_n)$  decreases according to (21) until it reaches its minimum at  $d_n = d_*$ . Our monotonicity assumption implies that  $|d_n^{1,2} - d_*|$  will monotonically decrease. Denote by  $\beta_{\max}(n)$  the value of  $\beta$  at which  $d_n = d_*$ . From (21) we find

$$\beta_{\max}(n) = -\alpha(n\pi)^4 - (n\pi)^2 f''(d_*)/2. \tag{23}$$

By (22), this expression is nonnegative. The value of  $n$  at which  $\beta_{\max}$  attains its maximum is

$$n_{\text{crit}} = \left\lfloor \frac{1}{\pi} \sqrt{\frac{|f''(d_*)|}{4\alpha}} \right\rfloor, \tag{24}$$

where  $\lfloor a \rfloor$  denotes the largest integer less than or equal to  $a$ . The largest possible value of  $\beta_{\max}$  equals

$$\beta_{\max}^{\max} = \beta_{\max}(n_{\text{crit}}) = (f''(d_*))^2/8\alpha. \tag{25}$$

Hence,  $\beta_{\max}(n)$  increases for  $n < n_{\text{crit}}$  and decreases for  $n > n_{\text{crit}}$ .

The maximum number of bifurcation points is determined by the condition  $\beta_{\max} = 0$ , which gives

$$n_{\max} = \left\lfloor \frac{1}{\pi} \sqrt{\frac{|f''(d_*)|}{2\alpha}} \right\rfloor. \tag{26}$$

Fig. 3 shows the curves  $\beta = -\alpha(n\pi)^4 - (n\pi)^2 f''(d)/2$  versus  $d$  for different values of  $n$  but fixed  $\alpha$ . In this case  $d_* = 0$  and the curves are parabolae. A horizontal line corresponding to a fixed value of  $\beta$  will intersect each fixed- $n$  curve at two bifurcation points  $d_n^1$  and  $d_n^2 = -d_n^1$ .

Observe an important difference with the no-foundation case  $\beta = 0$  (e.g. [20]). In that case, the bifurcation points are ordered:  $|d_n^{1,2}| < |d_m^{1,2}|$ ,  $n < m$ ;  $\max|d_n^{1,2}|$  is reached at  $n = 1$  and the corresponding branch has the lowest energy. These points are at the intersections of the curves in Fig. 3 and the  $\beta = 0$  line. In the pseudorigid foundation model, however, higher modes can bifurcate at lower values of  $E(d) - g(d)$  (total energy minus the elastic energy of the lower bar). For example, in Fig. 3, at  $\beta = 50$  one has  $d_{10}^2 > d_{15}^2 > d_4^2 > d_{20}^2$ . At  $\beta = 300$  one has  $d_{15}^2 > d_{10}^2 > d_{20}^2$  and solutions with low  $n \leq 4$  do not bifurcate from the trivial solution at all. Thus, solutions with a higher number of boundaries may have a lower energy. Fig. 5(a) shows an energy diagram obtained numerically, where solutions with  $n = 2$  have the lowest energy.

For **model I**, the analysis is similar. One obtains

$$\beta_{\max}(n) = \frac{(\pi n)^2 [-\alpha(\pi n)^2 - f''(d_*)/2]}{1 + [\alpha(\pi n)^2 + f''(d_*)/2]/\mu}. \tag{27}$$

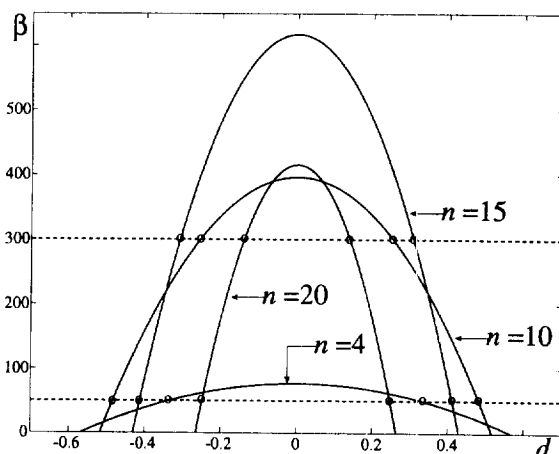


Fig. 3. Curves of the foundation constant  $\beta$  versus end displacement  $d$  for different  $n$ , for the pseudorigid foundation model. The points of intersection of the curves with  $\beta = \text{const.}$  are the bifurcation points.

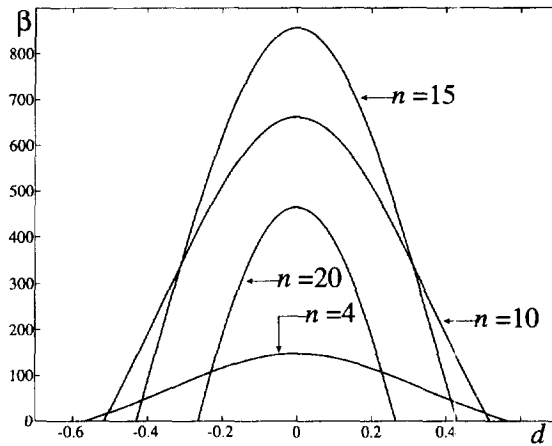


Fig. 4. Curves of the foundation constant  $\beta$  versus end displacement  $d$  for different  $n$ , for model I. The points of intersection of the curves with  $\beta = \text{const.}$  are the bifurcation points.

The maximum number  $n_{\text{max}}$  of bifurcation points is again given by (26) and hence is independent of  $\mu$  and  $\beta$ . If  $\mu > |f''(d_*)|/2$  and  $n \leq n_{\text{max}}$ , the expression (27) is nonnegative, and the maximum of  $\beta_{\text{max}}$  is reached at

$$n_{\text{crit}} = \left[ \frac{1}{\pi} \sqrt{\frac{\mu}{2\alpha}} \left( \frac{f''(d_*)}{\mu} + 2 \right)^{1/4} \sqrt{\sqrt{2} - \sqrt{\frac{f''(d_*)}{\mu} + 2}} \right]. \tag{28}$$

When  $\mu \leq |f''(d_*)|/2$ , the right-hand side of (27) is nonnegative for  $n_0 \leq n \leq n_{\text{max}}$  where

$$n_0 = \left[ \frac{1}{\pi} \sqrt{\frac{|f''(d_*)/2 + \mu|}{\alpha}} \right]. \tag{29}$$

In this case,  $\beta_{\text{max}}$  has its maximum value at  $n = n_0$  and decreases to zero at  $n = n_{\text{max}}$ .

The curves of  $\beta(d)$  for different  $n$  (with fixed  $\alpha$  and  $\mu > |f''(d_*)|/2$ ) are shown in Fig 4.

### 3. Symmetry

There are two types of symmetry in these models.

- (i) If  $(u_d, v_d)$  is an equilibrium solution for given  $d$  and the energy density satisfies  $f(-u') = f(u')$ , then the pair  $(z_{-d}, w_{-d}) = (-u_d, -v_d)$  is an equilibrium solution at  $-d$ , with the same energy. We refer to this as *physical symmetry* [19]. Thus the total energy is even:  $E(d) = E(-d)$ .
- (ii) Observe that if  $(u_d, v_d)$  satisfies the Euler–Lagrange equation (10), the natural boundary condition (11) and one of the sets of boundary conditions (7), (8) and (9) of models I, II or III, the same is true for  $(z_d(x), w_d(x)) = (-u_d(1-x), -v_d(1-x))$ , with the same total energy. Following the terminology of [19], we will say that these two solution pairs are related by *G-symmetry*.

Equilibrium solutions satisfying  $(u(x), v(x)) = (-u(1-x), -v(1-x))$  are called *G-symmetric*. In the pseudorigid foundation model and model I there is an additional symmetry, called *AG-symmetry*: if  $(u_d, v_d)$  is a G-symmetric solution, then  $(z_d, w_d)$  satisfying

$$z_d(x) = -u_d(1/2 - x) - d/2, \quad w_d(x) = -v_d(1/2 - x) - d/2, \quad 0 \leq x \leq 1/2 \tag{30}$$

and

$$z_d(x) = u_d(x - 1/2) + d/2, \quad w_d(x) = v_d(x - 1/2) + d/2, \quad 1/2 \leq x \leq 1 \tag{31}$$

is also an equilibrium with the same energy.

### 4. Numerical results on equilibrium solutions

In this section we present examples of equilibrium solutions for the above models.

Equilibria were found numerically using a pseudo-arclength continuation technique, implemented in the software package AUTO [5], with the end displacement  $d$  treated as a continuation parameter. The program follows the main branch of solutions, determines the bifurcation points, then calculates the bifurcating branches.

Stability was studied by considering the second variation of the energy functional. For the coupled-bar models it is given by

$$\delta^2 E(u_0, v_0; \eta, \xi) = \int_0^1 [f''(u_0)(\eta')^2 + 2\alpha(\eta'')^2 + 2\beta(\eta - \xi)^2 + 2\mu(\xi')^2] dx, \tag{32}$$

where  $(u_0, v_0)$  is an equilibrium and  $\eta \in H^2(0, 1)$ ,  $\xi \in H^1(0, 1)$  are admissible variations in  $u$  and  $v$ , respectively. These satisfy appropriate boundary conditions. For example, in model I with boundary conditions (7), we have  $\eta(0) = \eta(1) = \xi(0) = \xi(1) = 0$ . We approximate  $\eta$  and  $\xi$  by cubic Hermite polynomials, so that the second variation (32) is approximated by a finite sum, and numerically investigate the sign of the minimal eigenvalue of the resulting quadratic form.

The results are presented in two types of diagrams: total energy  $E(d)$  and effective stress  $S(d) = E'(d)$ . The arrangement of phases in the solutions is described by arrays of the symbols 0, +, - representing the spinodal and the  $\pm$  phases. For example, (+, 0, -) is an equilibrium in which the + and - phase occupy the left and the right parts of the bar, respectively, with the spinodal region between them. The stability of computed solutions is indicated in figure captions.

Consider the energy and stress diagrams for the pseudorigid foundation model shown in Figs. 5 and 6. In this model  $u = d(x - 1/2)$  is the trivial solution for each  $d$ . The 0-branch in Fig. 5 is the main branch consisting of these solutions. From this branch various nontrivial branches emerge with solutions locally given by (18) (in this case,  $n = 1, 2, 3$ ). In this example, we have chosen parameters so that the bifurcation points come in the order  $d_2^2 > d_1^2 > d_3^2$ . Here, as in Section 2, the lower index indicates the solution mode bifurcating. The points corresponding to  $d_2^2$ ,  $d_1^2$  and  $d_3^2$  in Fig. 5 are  $F, H$  and  $L$ . Points  $A, J$  and  $K$  correspond to  $d_2^1, d_1^1$  and  $d_3^1$ .

Consider the 2a-branch first. It bifurcates from the 0-branch at points  $A$  and  $F$ . Along this branch, stable

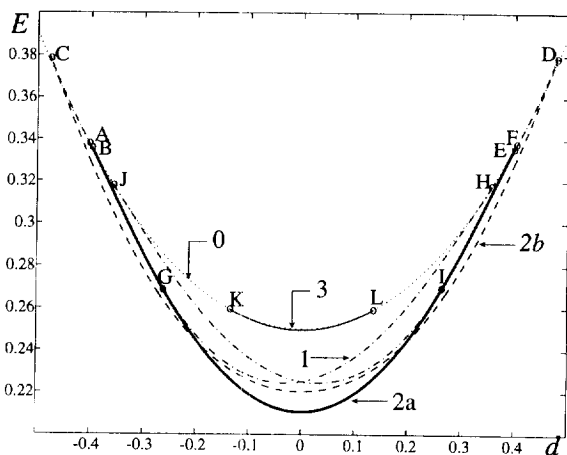


Fig. 5. Energy  $E(d)$  diagram for the pseudorigid foundation model:  $\alpha = 0.005, \beta = 2.5, g(d) = d^2$ ; 0:  $(-)\rightarrow(0)\rightarrow(+)$ , AF unstable, the rest is stable; 1:  $(0)\rightarrow(0, +)\rightarrow(0, -, 0, +)\rightarrow(0, -, 0)$ , unstable; 2a:  $(0)\rightarrow(+, 0, +)\rightarrow(+, 0, -, 0, +)\rightarrow(0, -, 0)\rightarrow(0)$ , G-symmetric, AB, GI and EF stable, BG and IE unstable; 2b:  $(0)\rightarrow(0, +, 0)\rightarrow(+, 0)\rightarrow(+, 0, -)\rightarrow(0, +, 0, -)\rightarrow(+, 0, -)\rightarrow(+, 0, -, 0)\rightarrow(+, 0, -)\rightarrow(0, -)\rightarrow(0, -, 0)\rightarrow(0, BC$  and  $DE$  unstable,  $CD$  stable; 3:  $(0), u'(x) - d$  has three zeroes, unstable.

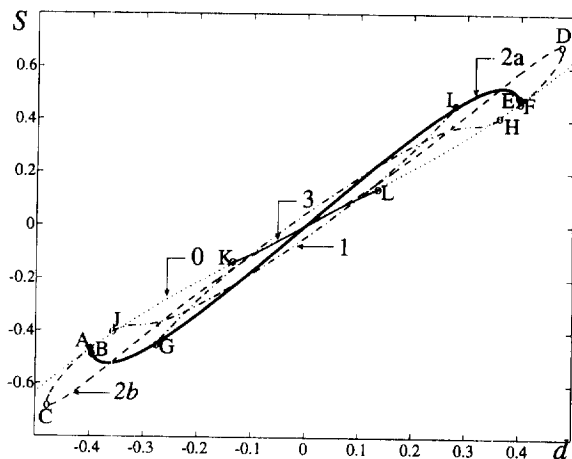


Fig. 6. Effective stress  $S(d)$  diagram for the pseudorigid foundation model:  $\alpha = 0.005, \beta = 2.5, g(d) = d^2$ . See the caption of Fig. 5.

G-symmetric solutions with two phase boundaries (+, 0, −, 0, +) develop. There are secondary bifurcations from the 2a-branch: these are the 1- and 2b-branches. The 2b-branch bifurcates at points B and E and consists of non-G-symmetric solutions, including some with one phase boundary. Observe that the 2a- and 2b-branches form the lowest energy envelope. Two 1-branches, HG and IJ, bifurcate from both the 0- and 2a-branches. The secondary bifurcations are due to the elastic foundation; they are not observed when  $\beta$  is small or zero. The 3-branch KL bifurcates from the 0-branch. Solutions along this branch have strain in spinodal region, although  $u'(x) - d$  has three zeroes. All branches except the 0-branch are run twice by solutions related by G- and AG-symmetry.

We now compare models I, II and III. The energy and stress diagrams are shown on Figs. 7, 8, 10 and 11. We have chosen the parameters  $\alpha$ ,  $\beta$  and  $\mu$  to be the same in all three models in order to isolate the effect of different boundary conditions.

In **model I**  $u = v = d(x - 1/2)$  is the trivial solution. The 0-branch in Fig. 7 consists of these solutions. In the example shown,  $\beta$  is relatively high, so there is only the 2-branch bifurcating at points A and B (along this branch  $u'(x) - d$  has two zeroes). Note that the higher mode (in this case it is  $n = 3$  since  $n_{max} = 3$  according to (26)) and the lower mode ( $n = 1$ ) primary bifurcations are absent as predicted by the local analysis. The 2-branch is run twice by solutions related by AG-symmetry.

The diagrams for **models II** and **III** are shown in Figs. 8 and 10, 11. In these models there is no trivial

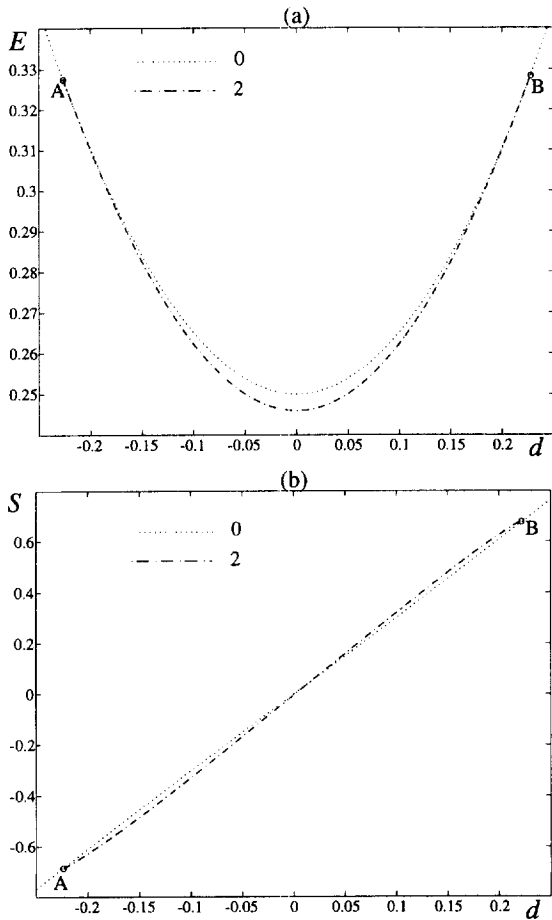


Fig. 7. (a) Energy  $E(d)$  and (b) effective stress  $S(d)$  diagrams for model I:  $\alpha = 0.005$ ,  $\beta = 10$ ,  $\mu = 2$ ; 0:  $(-)\rightarrow(0)\rightarrow(+)$ , AB unstable, the rest is stable; 2: (0), G-symmetric,  $u'(x) - d$  has two zeroes, stable.

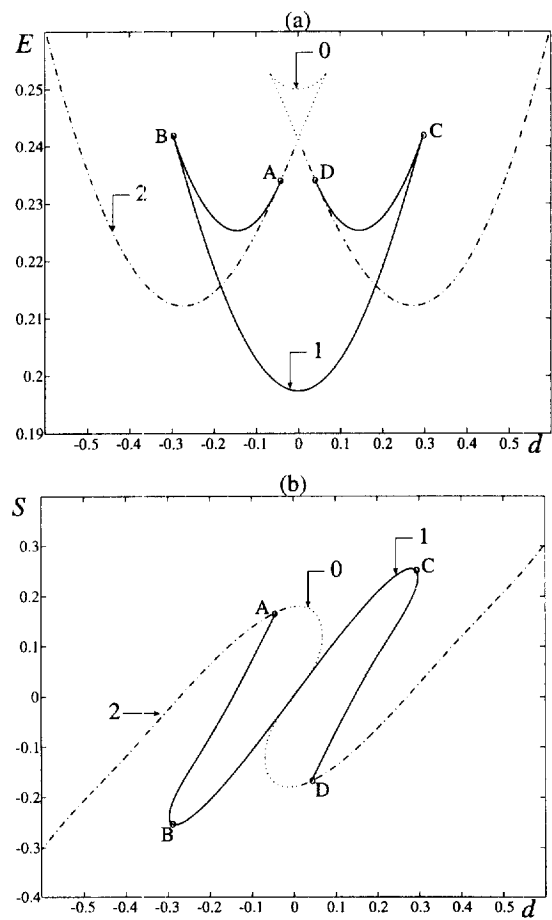


Fig. 8. (a) Energy  $E(d)$  and (b) effective stress  $S(d)$  diagrams in model II:  $\alpha = 0.005$ ,  $\beta = 10$ ,  $\mu = 2$ ; 0: (0), unstable; 1:  $(-, 0, -)\rightarrow(0, -)\rightarrow(+, 0, -)\rightarrow(+, 0, +)$ , BC stable, AB and CD unstable; 2:  $(-, 0, -)$ , solutions with  $d$  between A and D are unstable, the rest are stable. Solutions on 0- and 2-branches are G-symmetric.

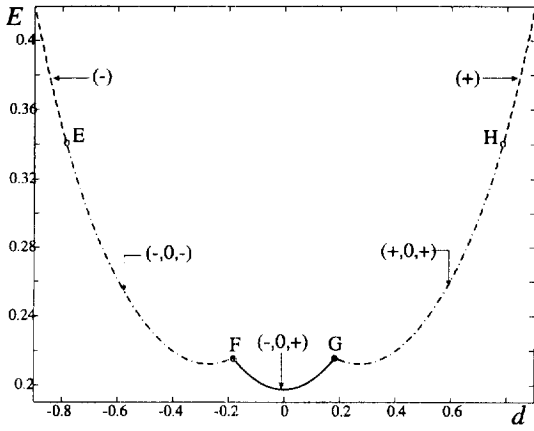


Fig. 9. The lowest energy envelope for model II:  $\alpha = 0.005$ ,  $\beta = 10$ ,  $\mu = 2$ .

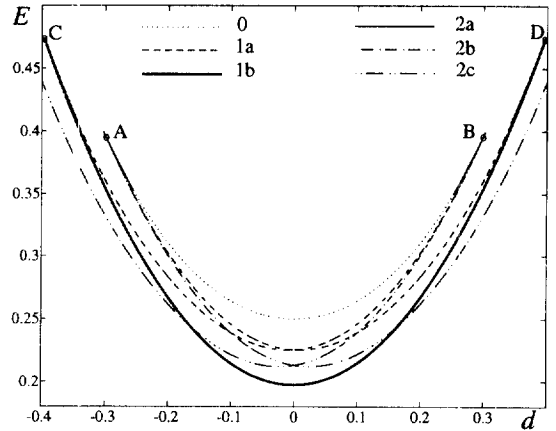


Fig. 10. Energy  $E(d)$  diagram for model III:  $\alpha = 0.005$ ,  $\beta = 10$ ,  $\mu = 2$ ; 0: (0), unstable; 1a: (0, -, 0)  $\rightarrow$  (+, 0, -)  $\rightarrow$  (+, 0), unstable; 1b: (+, 0, -), stable; 2a: (0, -, 0), unstable; 2b: (+, 0, -, 0, +), stable; 2c: (+, 0, +), stable. Solutions on 0-, 2a-, 2b- and 2c-branches are G-symmetric.

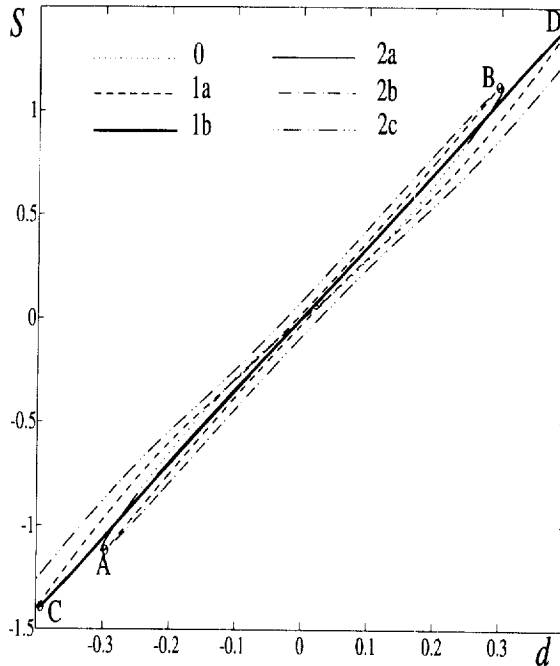


Fig. 11. Effective stress  $S(d)$  diagram for model III:  $\alpha = 0.005$ ,  $\beta = 10$ ,  $\mu = 2$ . See the caption of Fig. 10.

solution, and the main branch of solutions involves all G-symmetric solutions (0- and 2-branches in this case), while the non-G-symmetric bifurcating 1-branches are run over twice by G-symmetry-related solutions.

The lowest energy envelope for model II is shown in Fig. 9. If we start at  $d = -0.9$  and increase  $d$  following the lowest energy envelope, we observe the following sequence of phase transitions:  $(-)$   $\rightarrow$   $(-, 0, -)$   $\rightarrow$   $(-, 0, +)$   $\rightarrow$   $(+, 0, +)$   $\rightarrow$   $(+)$ . There are two kinds of phase nucleation events here. The transition  $(-, 0, -)$   $\rightarrow$   $(-, 0, +)$  is a *finite nucleation event*. By this we mean the following. Start with a  $(-, 0, -)$  solution and increase  $d$ , following the lowest energy envelope. When we approach point  $F$  from the left, a *finite* amount of  $+$  phase is suddenly born on the right after a finite amount of  $-$  phase denucleates. At point  $F$ , the solutions  $(-, 0, -)$  and  $(-, 0, +)$  are distant in the solution space, although their energies are the same (note, however, that the

effective stress drops at this point). In order to switch from one energy minimum to another, the system has to overcome a nonzero *energy barrier* (a ‘mountain pass’ between two minima). Such a transition is called a first-order phase transition. It corresponds to a corner on the lowest energy envelope. Another finite nucleation event occurs at point *G*. Points *E* and *H* correspond to a different kind of nucleation event—*infinitesimal phase nucleation*. If we start with a  $(-)$  solution and increase  $d$  following the lowest energy envelope, an infinitesimal amount of spinodal phase  $\theta$  is born in the *interior* of the bar as we approach point *E*. As we continue to increase  $d$ , the  $\theta$  interval grows inside the bar. This ‘pretransitional’ solution  $(-, 0, -)$  is stable although it contains a spinodal interval. The solutions  $(-)$  and  $(-, 0, -)$  are connected to each other at point *E*, and there is no energy barrier to overcome. This smooth connection on the lowest energy envelope is a characteristic of a second-order phase transition.

Both nucleation types occur in all three models and are similar to those observed when instead of the lower elastic bar there is a rigid substrate [20].

The coexistence of multiple metastable solutions at the same value of  $d$  suggests that *hysteresis* in the effective stress diagram is possible due to switching between branches. One can crudely estimate the form of hysteresis loops by estimating the energy barrier that the system must overcome in order to switch from one local energy minimum to another. We briefly describe and apply the method of barrier estimation that was introduced in [20]. Consider the energy diagram for model II shown in Fig. 12. Start from  $d = -1$  and increase  $d$ . Initially the entire bar is in the  $-$  phase, then the  $(-, 0, -)$ -branch is followed. Beyond point *F*, there are two stable solution branches— $(-, 0, -)$  and  $(-, 0, +)$ —coexisting for the range  $|d| < 0.2$ . Suppose that instead of following the lowest energy envelope, the system continues going along the stable  $(-, 0, -)$ -branch. Refer to this as solution 1. In order to switch from solution 1 to another local energy minimum, solution 2 on the  $(-, 0, +)$ -branch, the system must overcome an energy barrier (climb a certain ‘mountain pass’). This barrier corresponds to an unstable solution 3 of type  $(-, 0)$  connecting the two local minima. So the system first climbs from solution 1 to 3 and then falls to solution 2. The *energy barrier* is the difference in energies of solutions 1 and 3. The model from [20] requires this barrier to be less than or equal to a certain *critical barrier*  $B_{crit}$  for the switching to occur. In our calculations we choose  $B_{crit}$  to be zero. This means that the switching from  $(-, 0, -)$  to  $(-, 0, +)$  occurs at the bifurcation point *A* where the energy barrier is zero. This procedure results in a hysteresis loop shown in Fig. 13. Notice that the energy barrier that needs to be overcome in order to switch from the  $(-, 0, -)$ -branch to the  $(-, 0, +)$ -branch at point *F* is  $B = 0.01$ . Hence according to our criterion the system prefers to continue going along the metastable branch for a while instead of following the global minimum.

We remark that the pseudorigid foundation model and model I often exhibit little or no hysteresis for certain parameter ranges. For example, in Fig. 7 there is only one stable solution at each value of  $d$ . In contrast, models II and III show larger hysteresis loops due to coexistent metastable solutions. Examples are shown in Figs. 13 and 14. However, these loops are qualitatively different from the ones observed in experiments. For example, there are stress reversals in these loops that are not observed experimentally.

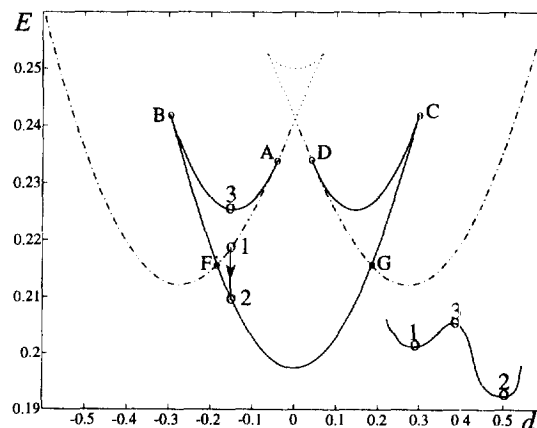


Fig. 12. Estimation of energy barriers: 1:  $(-, 0, -)$ , stable; 2:  $(-, 0, +)$ , stable; 3:  $(-, 0)$ , unstable.

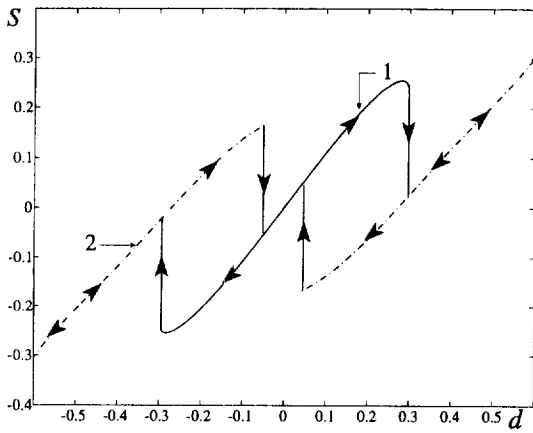


Fig. 13. Hysteresis loop for model II ( $\alpha = 0.005$ ,  $\beta = 10$ ,  $\mu = 2$ ) with  $B_{crit} = 0$ : 1: (+, 0, -); 2: (-, 0, -), G-symmetric.

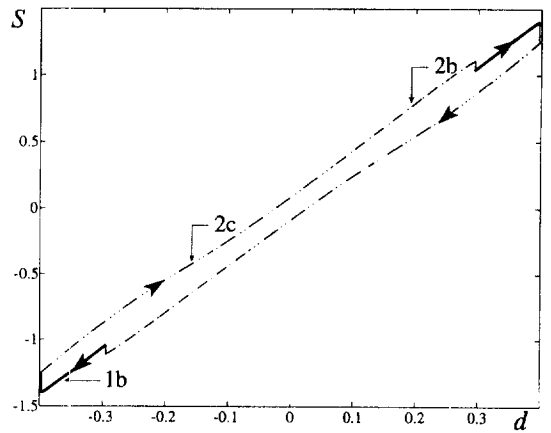


Fig. 14. Hysteresis loop for model III ( $\alpha = 0.005$ ,  $\beta = 10$ ,  $\mu = 2$ ) with  $B_{crit} = 0$ : 1b: (+, 0, -); 2b: (-, 0, +, 0, -), G-symmetric; 2c: (-, 0, -), G-symmetric.

### 5. The case of no interfacial energy

We now consider the case where interfacial energy is absent ( $\alpha = 0$ ), for which equilibria can be found analytically. For example, in model III we minimize the functional

$$E = \int_0^1 [f(u') + \mu v'^2 + \beta (u - v)^2] dx, \tag{33}$$

subject to

$$f'(u'(0)) = 0 \quad f'(u'(1)) = 0 \quad v(0) = -d/2 \quad v(1) = d/2. \tag{34}$$

We seek solutions with continuous displacements ( $u, v$ ) but possibly discontinuous strain  $u'$ . Assume that  $u'(x)$  has a finite number of finite jump discontinuities at isolated points  $x = c_i$ ,  $i = 1, n$ . Let  $c_0 = 0$  and  $c_{n+1} = 1$ . We are interested in solutions with strain  $u'$  alternating between the + and - phases, so that in each interval  $[c_i, c_{i+1}]$

$$f''(u') > 0. \tag{35}$$

Any solution containing a spinodal interval 0 (violating (35)) is unstable by the Legendre necessary condition [7]. The Euler–Lagrange equations become

$$\begin{cases} f''(u')u'' - 2\beta(u - v) = 0, \\ \mu v'' + \beta(u - v) = 0. \end{cases} \tag{36}$$

These should hold in each interval  $[c_i, c_{i+1}]$ , subject to (35). The Weierstrass–Erdman corner conditions [7] are

$$[[f'(u')]]_{c_i} = 0 \quad [[f(u') - f'(u')u']]_{c_i} = 0. \tag{37}$$

Here,  $[[A]]_c = A(c + 0) - A(c - 0)$  denotes the jump of the function  $A(x)$  at  $x = c$ . Conditions  $(37)_2$  stem from variations in  $c_i$ , while  $(36)$ , while  $(37)_1$  is obtained by varying  $u$  with  $c_i$  fixed.

We simplify the calculations by adopting the following piecewise quadratic energy density

$$f(u') = \begin{cases} f_+(u') = (u' + 1)^2 & \text{for } u' \leq -t, \\ f_0(u') = \gamma(u')^2 + \eta & \text{for } -t < u' < t, \\ f_-(u') = (u' - 1)^2 & \text{for } u' \geq t, \end{cases} \tag{38}$$

where

$$\gamma = 1 - 1/t < 0, \quad \eta = 1 - t$$

and  $t, -t$  are the points of contact of the three parabolae. The convex parabolae (graphs of  $f_{\pm}$ ) representing the

$\pm$  phases, are separated by a concave parabola on the spinodal region. The parameters  $\gamma$  and  $\eta$  are chosen so that  $f$  is  $C^1$ . This approximation of a fully nonlinear two-well energy density reduces (36) to a system of two linear equations with general solution

$$u(x) = a_{1,i}x + a_{2,i} + a_{3,i}e^{\tau x} + a_{4,i}e^{-\tau x} \tag{39}$$

and

$$v(x) = a_{1,i}x + a_{2,i} - (a_{3,i}e^{\tau x} + a_{4,i}e^{-\tau x})/\mu, \tag{40}$$

where  $\tau = \sqrt{\beta(1 + 1/\mu)}$ . Conditions (37) now reduce to the requirement that at each corner  $c_i$  the strain  $u'$  jumps from one Maxwell strain to another:

$$u'(c_i - 0) = \pm 1 \quad u'(c_i + 0) = \mp 1. \tag{41}$$

In addition, the smoothness conditions:

$$[[u]]_{c_i} = 0 \quad [[v]]_{c_i} = 0 \quad [[v']]_{c_i} = 0 \tag{42}$$

and the boundary conditions (34) should hold. The unknown coefficients  $a_{k,i}$ ,  $i = 0, \dots, n$ ,  $k = 1, \dots, 4$ , in (39) and (40) are then found from a system of  $4n + 4$  linear equations resulting from (41), (42)<sub>1,2</sub> and (34), as functions of  $d$ ,  $\beta$ ,  $\mu$  and  $c_i$ . Additional  $n$  nonlinear equations stemming from (42)<sub>3</sub> are solved to find  $c_i$ ,  $i = 2, \dots, n$ , and  $d$  in terms of  $c_1$ ,  $\mu$  and  $\beta$ .

A similar procedure applies to models I and II. Examples of resulting energy and stress diagrams for models II and III are shown in Figs. 15 and 16. Solutions shown here are weak local minimizers of the energy; they are

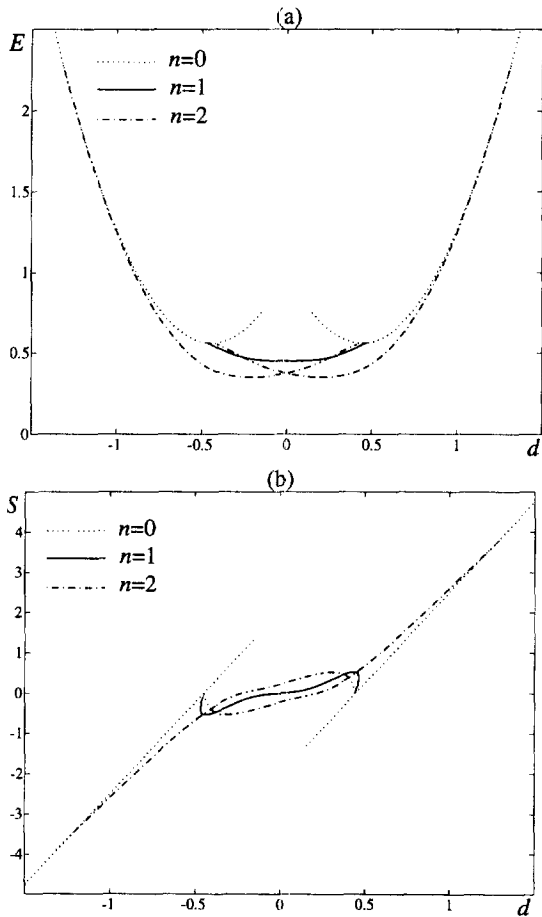


Fig. 15. (a) Energy  $E(d)$  and (b) effective stress  $S(d)$  diagrams for model II with no interfacial energy:  $\alpha = 0$ ,  $\beta = 100$ ,  $\mu = 2$ ,  $f(u')$  given by (38) with  $t = 0.1$ .

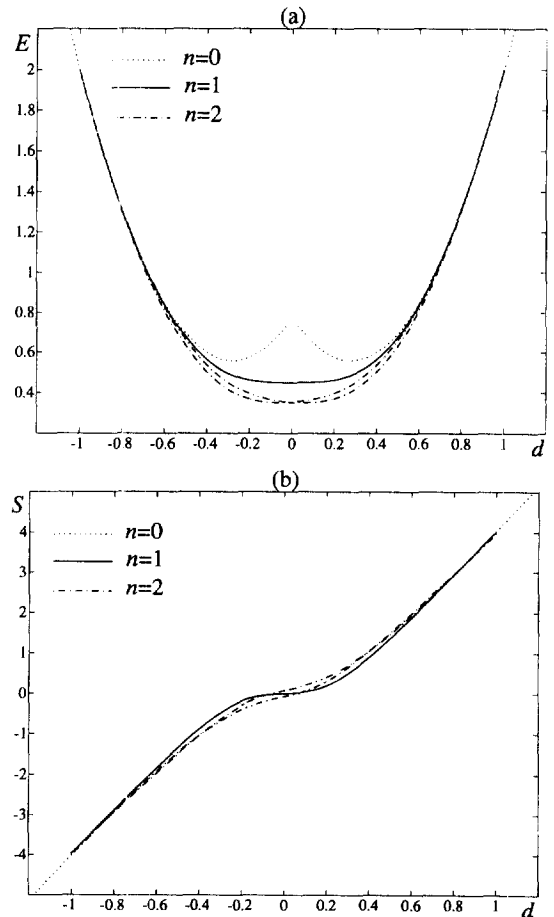


Fig. 16. (a) Energy  $E(d)$  and (b) effective stress  $S(d)$  diagrams in model III with no interfacial energy:  $\alpha = 0$ ,  $\beta = 100$ ,  $\mu = 2$ ,  $f(u')$  given by (38) with  $t = 0.1$ .

stable under  $C^1$  perturbations but unstable under perturbations in  $u$  which introduce new interfaces close to each other. The energy does not possess a global minimum. As  $n$  grows, the energy decreases, but it is possible to approach an infimum only as  $n \rightarrow \infty$ . Hence, the number of interfaces is unbounded in the absence of interfacial energy.

These calculations are useful not only because they involve an important limiting case  $\alpha = 0$  but also because one can combine them with (cruder) models of interfacial energy. For example, one can introduce an energy penalty for the formation of interfaces given by  $Cn$ , where  $C$  is a constant and  $n$  is the number of interfaces. Then solutions with some finite value of  $n$  that depends on  $C$  become global minimizers of the energy.

## 6. Conclusions

The one-dimensional phase transition models proposed and studied in this paper are admittedly crude when compared to more elaborate three-dimensional theories. Nonetheless, they capture certain important features of martensitic phase transitions, such as formation of finite-scale microstructures, phase nucleation and hysteresis.

Using the pseudo-arclength continuation technique, we numerically calculate bifurcation diagrams for equilibria. We find several branches of local minima coexisting for a range of the prescribed end displacement. Metastability of equilibria makes hysteretic behavior possible. Using the energetically motivated criterion for switching between branches of local energy minima introduced in [20], we predict hysteresis in the load–displacement diagrams resulting from our models.

As in [20], we observe two phase nucleation patterns. A finite phase nucleation event occurs when a finite amount of high strain phase suddenly nucleates in the bar that initially had strains in the low strain phase and spinodal region. Transitions of this kind are first-order phase transitions and require a certain energy barrier to be overcome before the system switches from one local energy minimum to another. The finite nucleation event corresponds to a corner on the lowest energy envelope. This was also observed in [19]. Another observed nucleation pattern is infinitesimal phase nucleation. This event happens when an infinitesimal interval with strains in the spinodal region appears in the interior of the bar that was initially in a low strain phase. This interval then gradually grows inside the bar. This process has some characteristics of a second-order phase transition, as it requires no energy barrier to overcome.

When displacement boundary conditions are prescribed for both bars, the model possesses a trivial solution with uniform strain and the bifurcation points of the nontrivial modes can be obtained analytically. For some parameter values we find that higher-mode solution branches bifurcate earlier than lower modes. Thus, solutions with a higher number of boundaries may have lower energy. Such a local analysis was not possible in [20], where the linearly elastic lower bar was replaced by a rigid substrate.

We find analytical solutions when the interfacial energy term is omitted. In this case the energy possesses no global minimum. Instead, it approaches an infimum as the number of phase boundaries grows unbounded.

While the present static approach yields various stable equilibria for the system, a dynamic analysis is needed in order to capture the appropriate mechanism of switching between branches of local energy minima. One may consider a model with inertia and viscosity effects. Such a study is undertaken in [21], and predicts various interesting phenomena not predictable by statics alone.

## Acknowledgment

This research was supported by the National Science Foundation through grants DMS-9625830, DMS-9704730 and DMS-9704509 (TJH) and MSS-9312858 (PR).

## References

- [1] R. Abeyaratne, C. Chu, and R.D. James, Kinetics and hysteresis in martensitic single crystals, in: *Mechanics of Phase Transformations and Shape Memory Alloys* (ASME, 1994).
- [2] J.M. Ball, P.J. Holmes, R.D. James, R.L. Pego and P.J. Swart, On the dynamics of fine structure, *J. Nonlinear Sci.* 1 (1991) 17–70.

- [3] J. Carr, M.E. Gurtin and M. Slemrod, Structured phase transitions on a finite interval, *Arch. Rat. Mech. Anal.* 86 (1984) 317–351.
- [4] C. Chu, Hysteresis and microstructures: A study of biaxial loading on compound twins of copper–aluminum–nickel single crystals, Ph.D. Thesis, University of Minnesota, 1993.
- [5] E.J. Doedel and J.P. Kerneves, AUTO: Software for continuation and bifurcation problems in ordinary differential equations (1986).
- [6] J.L. Ericksen, Equilibrium of bars, *J. Elasticity* 5 (1975) 191–202.
- [7] I.M. Gelfand and S.V. Fomin, *Calculus of Variations* (Prentice-Hall, Englewood Cliffs, NJ, 1963).
- [8] R.D. James, Deformation of shape-memory materials, in: C.Y. Liu, H. Kunsmann, K. Otsuka and M. Wuttig, eds., *Mat. Res. Soc. Symp. Proc.* Vol. 246 (1992) 81–90.
- [9] A.E. Lifshitz and G.L. Rybnikov, Dissipative structures and couette flow in a non-Newtonian fluid, *Sov. Phys. Dokl.* 30(4) (1985) 275–278.
- [10] S. Müller, Minimizing sequences for nonconvex functionals, phase transitions and singular perturbations, Vol. 359 of *Lecture Notes in Physics* (Springer, Berlin, 1990) 31–44.
- [11] S. Müller, Singular perturbation as a selection criterion for periodic minimizing sequences, *Calculus of Variations* 1 (1993) 169–204.
- [12] N. Nakanishi, Lattice softening and the origin of SME, in: J. Perkins, ed., *Shape Memory Effects in Alloys (AIME, 1975)* 147–175.
- [13] D. Schryvers, Y. Ma, L. Toth and L. Tanner, Nucleation and growth of bainitic Ni<sub>3</sub>Al<sub>1</sub> in B2 austenite, in: *PTM Solid-Solid Phase Transitions* (1994).
- [14] J.A. Shaw and S. Kyriakides, On the thermomechanical behavior of NiTi. Technical Report 94/12, EMRL, Department of Aerospace Engineering and Engineering Mechanics, The University of Texas at Austin, 1994.
- [15] T.W. Shield, Orientation dependence of the pseudoelastic behavior of single crystals of Cu-Al-Ni in tension, *J. Mech. Phys. Solids* 43(6) (1995) 869–895.
- [16] S.P. Timoshenko and J.M. Gere, *Theory of Elastic Stability* (McGraw-Hill Book Company, 1961).
- [17] N. Triantafyllidis and S. Bardenhagen, On higher order gradient continuum theories in 1-D nonlinear elasticity. Derivation from and comparison to the corresponding discrete models, *J. Elasticity* 33(3) (1993) 259–293.
- [18] L. Truskinovsky and G. Zanzotto, Finite-scale microstructures and metastability in one-dimensional elasticity, *Meccanica* 30 (1995) 577–589.
- [19] L. Truskinovsky and G. Zanzotto, Ericksen’s bar revisited: Energy wiggles, *J. Mech. Phys. Solids*, 44(8) (1996) 1371–1408.
- [20] A. Vainchtein, T. Healey, P. Rosakis and L. Truskinovsky, The role of the spinodal region in one-dimensional martensitic phase transitions, *Physica D*, 115 (1998) 29–48.
- [21] A. Vainchtein and P. Rosakis, Hysteresis and stick-slip motion of interfaces in dynamic models of phase transitions, *J. Nonlinear Sci.*, submitted.